frontiers | Frontiers in Physics

TYPE Original Research
PUBLISHED 29 November 2022
DOI 10.3389/fphy.2022.1091435

OPEN ACCESS

EDITED BY
Santosh Kumar,
Liaocheng University, China

REVIEWED BY
Dharmendra Kumar,
Madan Mohan Malaviya University of Technology, India
Jin Li,
Northeastern University, China

*CORRESPONDENCE
Weihua Shi,
njupt_shiwh@126.com

†These authors have contributed equally to this work

SPECIALTY SECTION
This article was submitted to Optics and Photonics, a section of the journal Frontiers in Physics

RECEIVED 07 November 2022
ACCEPTED 17 November 2022
PUBLISHED 29 November 2022

CITATION
Shi W, Mu R, Guo X, Jiang R, Shangguan M, Li QF, Zhang H, Zhang L and Wan H (2022), Double-parameter sensing of voltage and magnetic field based on photonic crystal fiber. *Front. Phys.* 10:1091435. doi: 10.3389/fphy.2022.1091435

Double-parameter sensing of voltage and magnetic field based on photonic crystal fiber

Weihua Shi*†, Rongqiu Mu†, Xiaochen Guo, Rushan Jiang, Mingyu Shangguan, Qing Feng Li, Huiyi Zhang, Ling Zhang and Hongdan Wan

College of Electronic and Optical Engineering and College of Flexible Electronics (Future Technology), Nanjing University of Posts and Telecommunications, Nanjing, China

In this paper, a new type of photonic crystal fiber (PCF) sensor is proposed for detecting the voltage and magnetic field simultaneously. In the PCF, an air hole of the cladding is coated with gold film and filled with the liquid crystal, thus the surface plasmon resonance (SPR) channel is formed to detect the voltage. While another air hole of the cladding is filled with magnetic fluids, the directional coupling channel is formed to detect the magnetic field. The SPR sensing channel and directional coupling channel are relatively independent. A finite element method (FEM) has been used for the optimization of the structure parameters, transmission characteristics of different modes, and analysis of the sensing characteristics. Numerical results reveal that the voltage sensitivity is 2.11 nm/V in the range of 5–35 V and the magnetic field sensitivity is 0.86 nm/Oe in the range of 90–210 Oe.

KEYWORDS

surface plasmon resonance, directional coupling, photonic crystal fiber, voltage, magnetic field, E7 nematic liquid crystal, sensor

Introduction

Electromagnetic fields are almost everywhere. Most of the equipments and systems are affected by their electromagnetic environment, especially in electrical industries, air, and rail transport [1]. The common electromagnetic sensors not only have poor detection accuracy but also are susceptible to electromagnetic interference [2]. Hence, there is an urgent need to develop highly sensitive, anti-electromagnetic interference systems to detect electromagnetic parameters.

Optical fiber sensors have many advantages, such as anti-electromagnetic interference, high-temperature resistance, corrosion resistance [3], etc. Photonic crystal fibers (PCFs) have their unique structures and performance, which make them significant in optical fiber sensing technology research [4–6].

Recently, PCFs have been used by many researchers in the development of electric and magnetic sensors. For sensing of the electric field or voltage, liquid crystal materials were filled in the different PCF structures, such as an all-fiber structure [7], a side-hole structure [8], and an all-polarization state structure [9]. For the sensing of magnetic field, magnetic

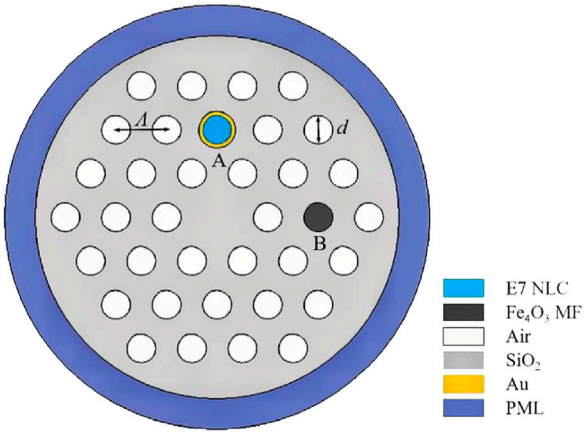

FIGURE 1
Cross section of PCF sensing structure.

fluid (MF) materials were filled in the PCFs, the different sensing mechanisms were used, such as surface plasmon resonance (SPR) [10, 11], directional coupling [12, 13], two-core coupling [14], Fabry-Perot (FP) interferometer [15, 16], Mach-Zehnder interferometer (MZI) [17, 18] and Sagnac interferometer [19].

However, these sensors typically operate as single-parameter sensors, the detection of electromagnetic parameters usually requires dual-parameter sensing. At present, the dual-parameter optical fiber sensors of the electric or magnetic fields are in the initial stage of theoretical and experimental research, in which one parameter is mostly temperature. Huang et al. [8] proposed a liquid-crystal-filled side-hole PCF to measure voltage and temperature. The sensitivity of voltage reached 3.88 nm/V, and the temperature sensitivity reached −1.5 nm/°C. Li et al. [18] proposed an in-line modal MZI based on a MF-filled PCF to measure the magnetic field and temperature. The sensitivity of the magnetic field reached 0.072 nm/Oe, and the temperature sensitivity reached 0.080/°C. However, these sensors also can't realize the simultaneous sensing of electric field and magnetic field, and the sensitivity and quality factor are to be further improved.

In this paper, a new type of voltage and magnetic field PCF sensor based on the mixed effects of SPR and directional coupling is proposed. The SPR channel is designed to detect the voltage and the directional coupling channel to detect the magnetic field. The numerical simulation demonstrates that the sensitivitives of voltage and magnetic field reaches 2.11 nm/V and 0.86 nm/Oe with good linearity respectively.

Design of voltage and magnetic field sensing structure

A cross-section diagram of the PCF electromagnetic sensing structure is shown in Figure 1. The fiber structure contains three layers of triangular-lattices arranged air holes with diameter d and lattice constant Λ. The thin gold film with thickness t is coated inside the air hole A, and an E7 nematic liquid crystal (NLC) is filled in the air hole A. The air hole A is used as an SPR channel to detect the voltage. Fe_4O_3 MF is filled in air hole B which is used as a directional coupling channel to detect the magnetic field.

When the applied voltage exceeds the threshold, molecules of the liquid crystal deflect an angle θ under the action of the electric field. The equation of the angle with the voltage V is [20]:

$$\theta = \begin{cases} 0, & V \le V_c \\ \frac{\pi}{2} - 2\tan^{-1}\left[\exp\left(-\frac{V - V_c}{30V_c}\right)\right], & V > V_c \end{cases} \quad (1)$$

where V_c is the threshold voltage and its value is $V_c = (\pi/2R)\sqrt{k_{11}/\Delta\varepsilon}$, k_{11} = 34pF, $\Delta\varepsilon$ = 10, $R = \Lambda/2$, Λ is the lattice constant of proposed sensing structure. At the same time, the refractive index of liquid crystal changes due to electro-optic effect, which can be expressed as [20]:

$$n_{NLC} = \begin{bmatrix} n' & 0 & 0 \\ 0 & n' & 0 \\ 0 & 0 & n'' \end{bmatrix}$$
$$\begin{cases} n' = n_{o1} \\ n'' = \dfrac{n_c n_{o1}}{\sqrt{n_c^2(\cos\theta)^2 + n_{o1}^2(\sin\theta)^2}} \end{cases} \quad (2)$$

Where n_{o1} is the ordinary refractive index of liquid crystal and n_c is the refractive index of air. Due to the anisotropy of NLC, n' and n'' are the refractive index at the different orientation. Thus, the refractive index of liquid crystal changes with the applied voltage.

The refractive index of MF is affected by the external magnetic fields and temperature. The relationship can be described by Langevin Equation [21]:

$$n_{MF}(H,T) = n_{o2} + [n_s - n_{o2}] \times \left[\cosh\left(\alpha\frac{H - H_{cn}}{T}\right) - \frac{T}{H - H_{cn}}\right], H > H_{cn} \quad (3)$$

Where H is the intensity of the magnetic field, H_{cn} is the threshold value of the magnetic field, T is the temperature and α is the fitting parameter. n_{o2} is the refractive index of the MF with no external magnetic field (or the magnetic field strength is less than the threshold value). Besides, n_s is the saturated refractive index when the magnetic field increases to a certain degree, n_{o2} and n_s are constants only related to magnetic fluid materials.

The base material of the sensor is silicon dioxide (SiO_2). The refractive index of SiO_2 can be obtained by the Sellmeier formula [22]:

$$n_{SiO_2}^2(\lambda) = 1 + \frac{B_1\lambda^2}{\lambda^2 - C_1} + \frac{B_2\lambda^2}{\lambda^2 - C_2} + \frac{B_3\lambda^2}{\lambda^2 - C_3} \quad (4)$$

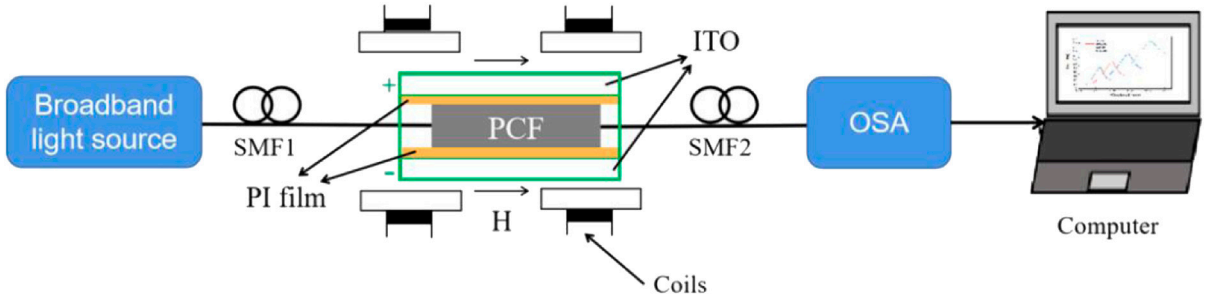

FIGURE 2
Simulation experimental system of the proposed sensing structure.

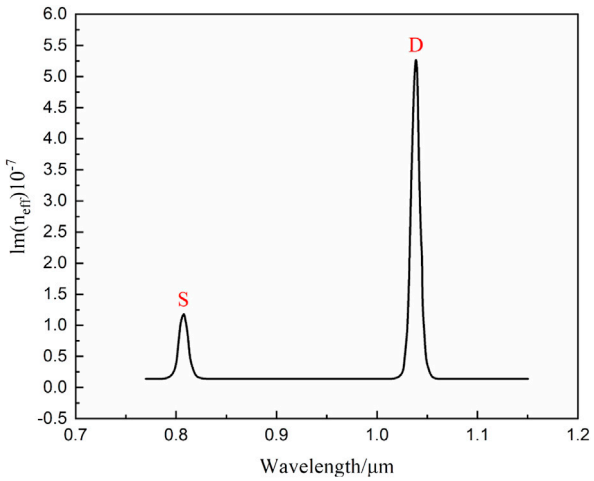

FIGURE 3
The loss curves of SPR and directional coupling channels.

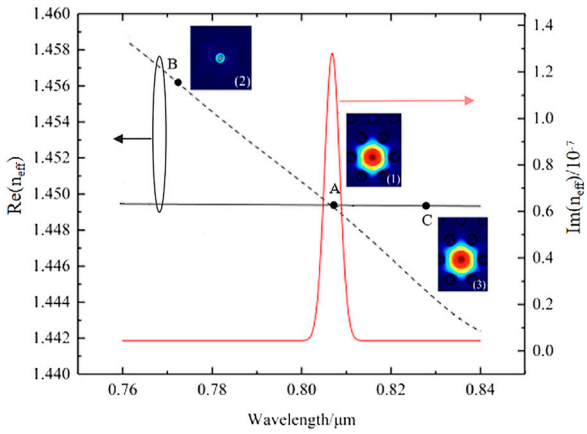

FIGURE 4
Dispersion characteristics (black solid line) and loss characteristics (red solid line) of core mode, as well as the dispersion characteristics (dotted black line) of SPP mode. (Illustrations (1) and (3) are the field distributions of core mode at points **(A,C)**. Illustration (2) is the field distribution of SPP mode at point **(B)**.).

Where, λ is the wavelength of incident light, $B_1 = 0.696163$, $B_2 = 0.4079426$, $B_3 = 0.8974794$, $C_1 = 4.67914826 \times 10^{-3}$, $C_2 = 1.35120631 \times 10^{-2}$, and $C_3 = 97.9340025$.

The dielectric constant of gold is derived from the Drude model [23]:

$$\varepsilon_{Au} = \varepsilon_{\infty} - \frac{\omega_D^2}{\omega(\omega + j\gamma D)} - \frac{\Delta\varepsilon\Omega_L{}^2}{(\omega^2 - \Omega_L{}^2) + j\Gamma_L\omega} \quad (5)$$

Where, ε_{Au} refers to the permittivity of gold, ε_{∞} represents the permittivity at high frequency with a value of 5.9673. ω_D is the plasma frequency and $\omega_D/2\pi = 2113.6$ THz γ_D is the damping frequency, $\gamma_D/2\pi = 15.92$ THz. The angular frequency can be expressed as $\omega = 2\pi c/\lambda$, c is the velocity of light in vacuum. $\Delta\varepsilon = 1.09$, $\Gamma_L/2\pi = 104.86$ THz, and $\Omega_L/2\pi = 650.07$ THz.

Figure 2 is the simulation experimental system of the proposed sensing structure. A voltage is applied along the PCF section direction and a magnetic field is applied radially along the PCF. The proposed PCF is connected with two single-mode fibers (SMFs), which can be considered as a bridge between broadband light and optical spectrum analyzer (OSA). The incident light passes through the PCF sensing structure and finally obtains the loss characteristics in OSA. The applied voltage and magnetic field can be detected by numerical analysis.

Results and discussion

Numerical simulation of the proposed PCF sensing structure is gotten by the finite element method (FEM) with perfectly matched layer boundary conditions.

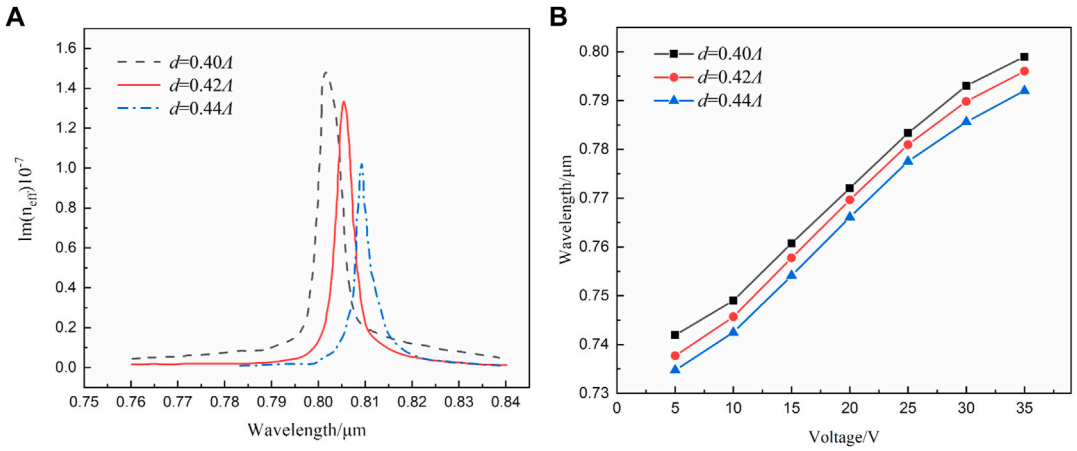

FIGURE 5
Influence of different air hole diameter *d* on sensing characteristics under SPR effect by setting *N* = 3, Λ = 8 μm, *t* = 40 nm. **(A)** The loss curves of core mode for different *d*. **(B)** The resonance wavelength with voltage for different *d*.

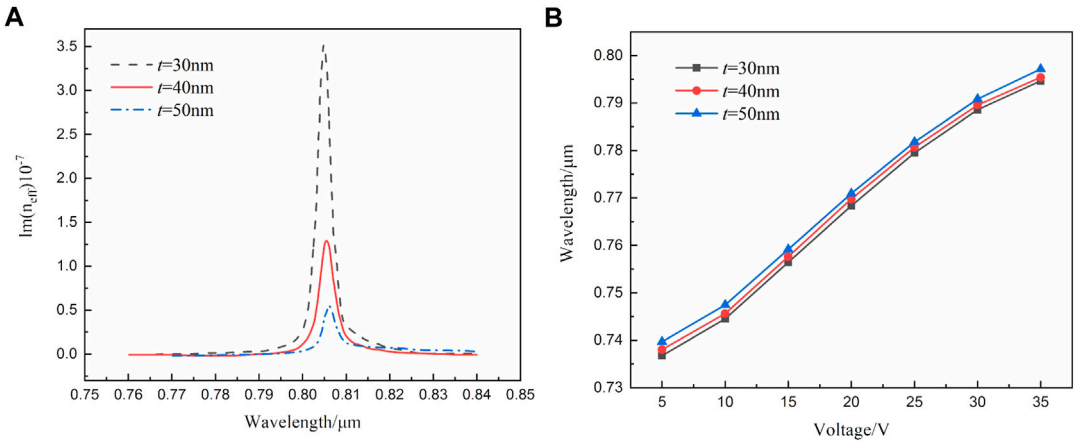

FIGURE 6
Influence of Au thickness *t* on sensing characteristics under SPR effect by setting *N* = 3, Λ = 8 μm, *d* = 0.42Λ. **(A)** The loss curves of core mode for different *t* **(B)** The resonance wavelength with voltage for different *t*.

The surface plasmon polariton (SPP) mode and defect mode of the PCF resonate with the core mode, respectively, to generate two separate loss peaks in the optical fiber spectrum, as shown in Figure 3. NLC and MF are selectively filled in the PCF. The change of the refractive index in the PCF, which is caused by the applied voltage and magnetic field, leads to the displacements of the loss peaks. The displacements of the loss peaks can be analyzed to realize the electromagnetic double-parameter sensing.

The loss characteristics of PCF are analyzed by the imaginary part Im (n_{eff}) of the effective refractive index n_{eff} in core mode, as shown in Figure 3, where the temperature is 25°C, the magnetic field intensity is 210 Oe, and the voltage is 35 V. From Figure 3, it can be seen that there are two separate resonance loss peak S and D in the near-infrared spectroscopy (NIR). Loss peak S is at 0.805 μm and is controlled by the SPR channel for voltage sensing. Loss peak D is at 1.037 μm and is controlled by the directional coupling channel for magnetic field sensing.

Through numerical simulation, it is found that the relative position of the resonance peak of the directional coupling magnetic field sensing does not vary with the influence of the SPR sensing channel. In addition, the SPR voltage sensing is not

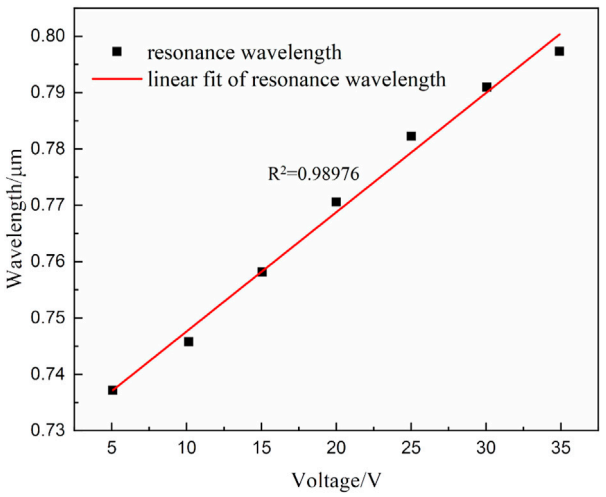

FIGURE 7
Resonance wavelength versus voltage.

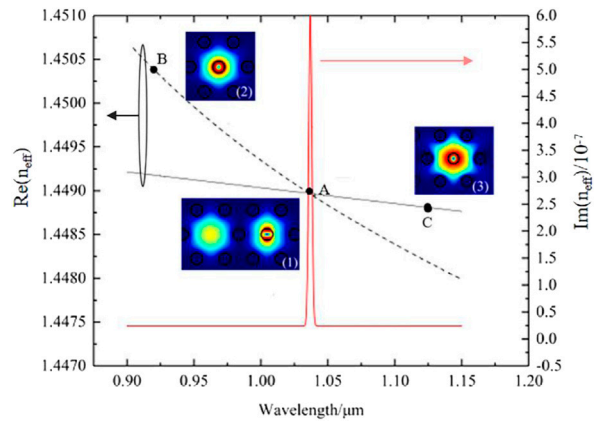

FIGURE 8
Dispersion characteristics (black solid line) and loss characteristics (red solid line) of core mode, as well as the dispersion characteristics (dotted black line) of defect mode in directional coupling channel. [Illustrations (1) is the field distributions of core mode and defect mode at point **(A)**. Illustration (2) is the field distribution of directional coupled-mode at point **(B)**. Illustrations (3) is the field distributions of core mode at point **(C)**].

affected by the directional coupling sensing channel. Hence, the SPR sensing channel and the directional coupling sensing channel are relatively independent.

The structural parameters of the proposed sensing structure have a great influence on confinement loss and sensing properties. The main parameters of PCF affecting the double-parameter sensing properties are the number of air hole layers (N), the lattice constant (Λ), the air hole diameter (d), and the gold film thickness (t). Among these, the lattice constant Λ and the number of air hole layers N have been calculated to have almost no effect on sensing performance. Therefore, N is determined to be 3 and Λ to be 8 μm. On this basis, the influence of d, and t on voltage and magnetic field double-parameter sensing are analyzed in the following sections.

Analysis of voltage sensing characteristics

Dispersion characteristics and loss characteristics of core mode, as well as the dispersion characteristics of SPP mode, are shown in Figure 4, where the temperature is 25°C, the magnetic field intensity is 210 Oe, and the voltage is 35 V. When the resonance matching condition is satisfied between core mode and SPP mode at the point A, the energy is transferred from core mode to SPP mode, the SPR effect occurs. The loss of core mode increases and finally reaches the maximum. Hence, a narrow loss peak at resonance wavelength of 0.805 μm occurs. The corresponding field distribution of core mode is shown in Figure 4(1). When $n_{eff}^{c} < n_{eff}^{s}$, the resonance matching condition is not satisfied at the point B, the energy will be concentrated in the fiber core. The corresponding distribution of the core mode is shown in Figure 4(3). Here, n_{eff}^{s} is the real part of the effective refractive index of SPP mode, $n_{eff}^{c}$is the real part of the effective refractive index of core mode. When $n_{eff}^{c} > n_{eff}^{s}$, the energy is limited in the SPP mode at the point C, and the corresponding distribution of the SPP mode is shown in Figure 4(2).

Figure 5A shows the loss curves of core mode under SPR effect for air hole diameters d of 0.40Λ, 0.42Λ, and 0.44Λ, respectively. As can be seen, the resonance matching point is shifted towards a longer wavelength with the increase of cladding air holes. At the same time, the loss peak and the full width at half-maximum (FWHM) both reduced significantly. Figure 5B shows the variation of resonance wavelength with voltage for different d. The voltage sensing sensitivity is 2.06 nm/V, 2.11 nm/V, and 2.07 nm/V when d is 0.40Λ, 0.42Λ, and 0.44Λ, respectively. On balance, it is determined that the SPR effect-based voltage sensing is best achieved with an air hole diameter of d = 0.42Λ.

The influence of the gold film thickness t on the voltage sensing characteristics under SPR effect is then discussed. The loss curves of core mode for gold film thicknesses t of 30 nm, 40 nm, and 50 nm are shown in Figure 6A, respectively. As t increases, the loss peak decreases significantly. This is due to the thickened gold film absorbing the energy propagating from the fiber core to the cladding. As a result, the liquid crystal gains very weak energy in air hole A, which weakens the SPR resonance strength and reduces the loss peak. Figure 6B shows the variation of resonance wavelength with voltage for different t. The voltage sensing sensitivity is almost equal for different t. After

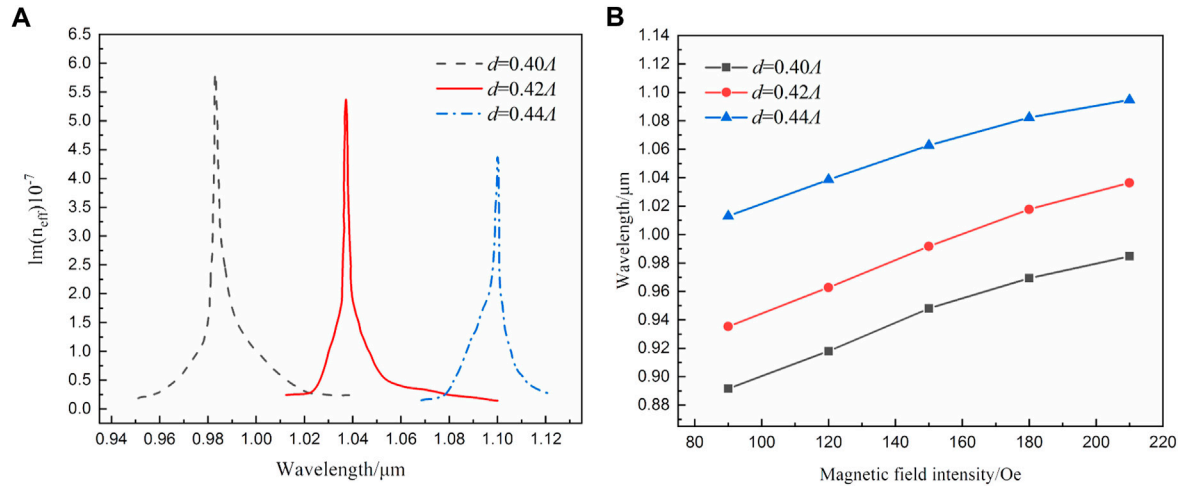

FIGURE 9
Influence of different air hole diameter *d* on sensing characteristics under directional coupling effect by setting $N = 3$, $\Lambda = 8$ μm, $t = 40$ nm. **(A)** The loss curves of core mode for different *d*. **(B)** The resonance wavelength with magnetic field intensity for different *d*.

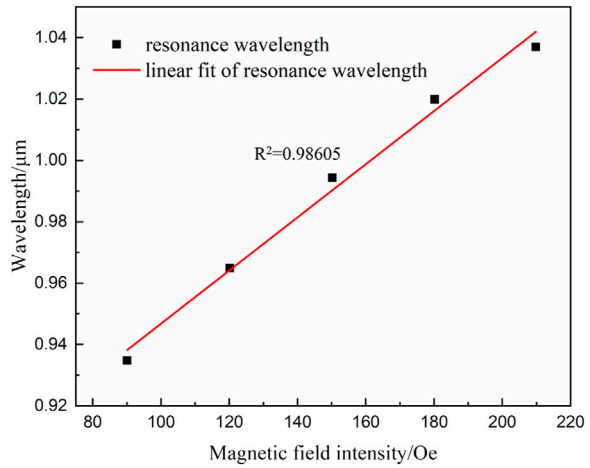

FIGURE 10
Resonance wavelength versus magnetic field intensity.

comprehensive consideration, the final gold film thickness is determined as $t = 40$ nm.

The refractive index of E7 NLC is changed with applied voltage, the matching position between the core mode and defect mode is changed, which makes shifting of the loss peak of the core mode in the PCF. Therefore, the voltage can be measured indirectly from the position of the core mode's loss peak. The voltage sensitivity can be obtained by calculating the shift of the resonance wavelength, which is expressed as:

$$Sv\,(nm/V) = \frac{\Delta\lambda}{\Delta V} \tag{6}$$

TABLE 1 Performance comparison of the proposed sensor with other recent reported PCF sensors.

References	Parameters	Sensitivity	Mechanism
[11]	Magnetic field	0.087 nm/Oe	SPR
[18]	Magnetic field	0.072 nm/Oe	MZI
	Temperature	−0.080 nm/°C	
[24]	Electric field	0.143 V/m	MZI
[25]	Voltage	1.29 nm/V	Resonance coupling
[26]	Voltage	0.971 nm/V	Directional coupling
This work	Voltage	2.11 nm/V	SPR
	Magnetic field	0.86 nm/Oe	Directional coupling

where $\Delta\lambda$ represents the variation of resonance wavelength and ΔV represents the variation of external voltage.

At the situation of 25°C and 210 Oe, the relationship between resonant wavelength and voltage is shown in Figure 7, by setting $N = 3$, $\Lambda = 8$ μm, $d = 0.42\Lambda$, $t = 40$ nm. The loss peak has a redshift with increasing voltage. In the voltage range of 5–35 V, the voltage sensitivity of the proposed PCF sensor is 2.11 nm/V and the linearity is 0.98976.

Analysis of magnetic field sensing characteristics

Dispersion characteristics and loss characteristics of core mode, as well as the dispersion characteristics of defect mode in directional

coupling channel, are shown in Figure 8, where the temperature is 25°C, the magnetic field intensity is 210 Oe, and voltage is 35 V. When the wave vector matching condition is satisfied between core mode and defect mode at the point A, the energy is mostly transferred from core mode to defect mode, the directional coupling effect occurs. The loss of core mode increases and finally reaches the maximum. Hence, a narrow loss peak at resonance wavelength of 1.037 μm occurs. The corresponding field distributions of the core mode and defect mode at the directional coupled state are shown in Figure 8(1). When $n_{eff}^{c} < n_{eff}^{d}$, the wave vector matching condition is not satisfied at the point B, the energy is concentrated in the core. The corresponding distribution of the defect mode is shown in Figure 8(2). Here, n_{eff}^{d} is the real part of the effective refractive index of defect mode. When $n_{eff}^{c} > n_{eff}^{d}$, the energy is limited in the defect mode at the point C, the corresponding distribution of the core mode is shown in Figure 8(3).

Figure 9A shows the loss curves of core mode for air hole diameters d of 0.40Λ, 0.42Λ, and 0.44Λ under directional coupling effect, respectively. With the increase of diameter d, the resonance wavelength shifts toward longer wavelength while the FWHM remains. Figure 9B shows the variation of resonance wavelength with magnetic field for different d. The magnetic field sensing sensitivity is 0.79 nm/Oe, 0.86 nm/Oe, and 0.68 nm/Oe when the air hole diameters d is 0.40Λ, 0.42Λ, and 0.44Λ, respectively. After comprehensive consideration, the final gold film thickness is determined as d is 0.42Λ.

Thus magnetic field can be measured indirectly from the position of the core mode's loss peak. The magnetic field sensitivity can be obtained by calculating the shift of the resonance wavelength, which is expressed as:

$$S_H\left(nm/\mathrm{Oe}\right) = \frac{\Delta\lambda}{\Delta H} \tag{7}$$

where $\Delta\lambda$ represents the variation of resonance wavelength and ΔH represents the variation of external magnetic field.

At the situation of 25°C and 35 V, the relationship between resonant wavelength and magnetic field intensity is shown in Figure 10 by setting $N = 3$, $\Lambda = 8$ μm, $d = 0.42\Lambda$, $t =$ 40 nm. The loss peak has a redshift with increasing magnetic field intensity. In the magnetic field range of 90–210 Oe, the magnetic field sensitivity of the proposed PCF sensor is 0.86 nm/Oe and the linearity is 0.98605.

Table 1 shows a comparative study between the proposed design and other sensors reported in recent years in terms of sensing performance. It can be seen that PCF electromagnetic sensing structure in this paper has a higher sensitivity and is able to detect voltage and magnetic field double-parameter.

Conclusion

A novel electromagnetic double-parameter PCF sensing structure combined with the SPR effect and directional coupling effect has been proposed in this paper. NLC is filled in a gold-coated air hole to form the SPR channel for voltage sensing detection. MF is filled in another air hole to form the directional coupling channel for magnetic field sensing detection. The SPP mode and defect mode of the PCF resonate with the core mode respectively, to generate two independent loss peaks in the optical fiber spectrum. It can be seen that in the range of 5–35 V and 90–210 Oe, the sensitivities of voltage and magnetic field reach 2.11 nm/V and 0.86 nm/Oe respectively with good linearity. The electromagnetic dual-parametric sensing structure designed in this paper has the advantages of simple structure and the ability to achieve simultaneous independent sensing of both voltage and magnetic field. The proposed dual-parametric sensing structure has potential application prospects in electromagnetic environment monitoring.

Data availability statement

The raw data supporting the conclusion of this article will be made available by the authors, without undue reservation.

Author contributions

WS: Supervision, project administration, writing review and editing. RM: Writing-review, project administration, data curation and editing. XG: Writing-original draft. RJ: Writing-review and editing. MS: Writing-review and editing. QL: Writing-review and editing. HZ: Writing-review and editing. LZ: Writing-review and editing. HW: Funding acquisition. All authors have read andagreed to the published version of the manuscript.

Funding

This work was supported in part by National Natural Science Foundation of China under Grant 61571237, and in part by General program of Natural Science Foundation of Jiangsu Province under Grant BK20221330.

Conflict of interest

The authors declare that the research was conducted in the absence of any commercial or financial relationships that could be construed as a potential conflict of interest.

Publisher's note

All claims expressed in this article are solely those of the authors and do not necessarily represent those of their affiliated

organizations, or those of the publisher, the editors and the reviewers. Any product that may be evaluated in this article, or claim that may be made by its manufacturer, is not guaranteed or endorsed by the publisher.

References

1. Christoforidis GC, Papadopoulos TA, Parisses C, Mantzaras GE. Photovoltaic power plants as a source of electromagnetic interference to metallic agricultural pipelines. *Proced Technol* (2013) 8(3):192–9. doi:10.1016/j.protcy.2013.11.027

2. Peng J, Jia SH, Bian JM, Zhang S, Liu J, Zhou X. Recent progress on electromagnetic field measurement based on optical sensors. *Sensors* (2019) 19(13):2860. doi:10.3390/s19132860

3. Gordon KL. Thermometry and dosimetry of heat with specific reference to the liquid-crystal optical fiber temperature probe. *Radiat Environ Biophys* (1980) 17(3): 233–43. doi:10.1007/BF01323650

4. Chaudhary VS, Kumar D, Kumar S. Gold-immobilized photonic crystal fiber-based SPR biosensor for detection of malaria disease in human body. *IEEE Sens J* (2021) 21(16):17800–7. doi:10.1109/JSEN.2021.3085829

5. Mishra GP, Kumar D, Chaudhary VS, Kumar S. Design and sensitivity improvement of microstructured-core photonic crystal fiber based sensor for methane and hydrogen fluoride detection. *IEEE Sens J* (2021) 22(2):1265–72. doi:10.1109/JSEN.2021.3131694

6. Chaudhary VS, Kumar D, Kumar S. Au-TiO_2 coated photonic crystal fiber based SPR refractometric sensor for detection of cancerous cells. *IEEE Trans Nanobioscience* (2022) 1. doi:10.1109/TNB.2022.3219104

7. Meng QY, Ren GH. Experimental study on electric field sensing of reflective doped liquid crystal photonic crystal fiber. *J Optoelectonics·Laser* (2012) 23(9): 1713–6. doi:10.16136/j.joel.2012.09.005

8. Huang YJ, Wang Y, Mao C, Wang J, Wu H, Liao C, et al. Liquid-crystal-filled side-hole fiber for high-sensitivity temperature and electric field measurement. *Micromachines* (2019) 10(11):761. doi:10.3390/mi10110761

9. Liu H, Wu CQ, Lan SF, Yang W. Suspended optical fiber voltage sensor based on all polarization state detection. *Acta Photonica Sinca* (2014) 43(7):706016. doi:10.3788/gzxb20144307.0706016

10. Wang JK, Ying Y, Gao ZJ, Cheng SY, Si GY. Surface plasmon resonance (SPR) based temperature and magnetic field sensor in a dual-core D-shaped photonic crystal fiber (PCF). *Instrumentation Sci Technol* (2021) 1(17):271–87. doi:10.1080/10739149.2021.1994417

11. Islam MR, Khan MMI, Siraz S, Islam M, Mehjabin F, Rahman M, et al. Design and analysis of a QC-SPR-PCF sensor for multipurpose sensing with supremely high FOM. *Appl Nanosci* (2022) 12(1):29–45. doi:10.1007/s13204-021-02150-6

12. Liu H, Wang Q, Ding Y, Li HW, Wang M, Wang HR, et al. Concurrent measurements of temperature and magnetic-field based on the combined use of modal interference and directional coupling in photonic crystal fiber. *Optik* (2019) 179:62–70. doi:10.1016/j.ijleo.2018.10.132

13. Liang Y, Zhang H, Guo H, Wang Y, Gao Y, Ma H, et al. Simultaneous measurement of temperature and magnetic field based on directional resonance coupling in photonic crystal fibers. *Opt Commun* (2017) 391:111–5. doi:10.1016/j.optcom.2017.01.024

14. Zhang YJ, Wang LZ, Jia PG, Zhu F, Zhai C, Liu L, et al. High-sensitivity refractive index sensor with cascaded dual-core photonic crystal fiber based on vernier effect. *Optik* (2022) 256:168488. doi:10.1016/j.ijleo.2021.168488

15. Zhao Y, Lv RQ, Ying Y, Wang Q. Hollow-core photonic crystal fiber Fabry-Perot sensor for magnetic field measurement based on magnetic fluid. *Opt Laser Technol* (2012) 44(4):899–902. doi:10.1016/j.optlastec.2011.11.011

16. Greice KBC, Gouvêa PMP, Soares LMB, JoãoPereira MB, Favero F, ArthurBraga MB, et al. In-fiber Fabry-Perot interferometer for strain and magnetic field sensing. *Opt Express* (2016) 24(13):14690–6. doi:10.1364/OE.24.014690

17. Taghizadeh M, Bozorgzadeh F, Ghorbani M. Designing magnetic field sensor based on tapered photonic crystal fibre assisted by a ferrofluid. *Sci Rep* (2021) 11(1): 14325. doi:10.1038/s41598-021-93568-z

18. Li XG, Zhou X, Zhao Y, Lv RQ. Multi-modes interferometer for magnetic field and temperature measurement using Photonic crystal fiber filled with magnetic fluid. *Opt Fiber Technol* (2018) 41(9):1–6. doi:10.1016/j.yofte.2017.12.002

19. Zhao Y, Wu D, Lv RQ, Li J. Magnetic field measurement based on the sagnac interferometer with a ferrofluid-filled high-birefringence photonic crystal fiber. *IEEE Trans Instrum Meas* (2016) 65(6):1503–7. doi:10.1109/TIM.2016.2519767

20. Wu T, Yang D, Liu Z, Yang Z, Cao W, Wang Y. Multifunctional optoelectronic device based on liquid crystal selectively filled flat-plate photonic crystal fiber. *Optik* (2021) 250:168328. doi:10.1016/j.ijleo.2021.168328

21. Hong CY, Horng HE, Yang SY. Tunable refractive index of magnetic fluids and its applications. *Phys Stat Sol* (2004) 1(7):1604–9. doi:10.1002/pssc.200304388

22. Malitson IH. Interspecimen comparison of the refractive index of fused silica. *J Opt Soc Am* (1965) 55(10):1205–9. doi:10.1364/josa.55.001205

23. Vial A, Grimault AS, Macías D, Barchiesi D, de la Chapelle ML. Improved analytical fit of gold dispersion: Application to the modeling of extinction spectra with a finite-difference time-domain method. *Phys Rev B* (2005) 71(8):085416. doi:10.1103/physrevb.71.085416

24. Zhao Y, Zhang YN, Lv RQ, Li J. Electric field sensor based on photonic crystal cavity with liquid crystal infiltration. *J Lightwave Technol* (2017) 35(16):3440–6. doi:10.1109/JLT.2016.2576500

25. Wang WL, Liu Q, Liu ZY, Wu Q, Fu YQ. Simulation of a temperature-compensated voltage sensor based on photonic crystal fiber infiltrated with liquid crystal and ethanol. *Sensors* (2022) 22(17):6374. doi:10.3390/s22176374

26. Yang D, Wu T, Wang Y, Cao W, Zhang H, Liu Z, et al. A multi-parameter integrated sensor based on selectively filled D-shaped photonic crystal fiber. *Materials* (2022) 15:2811. doi:10.3390/ma15082811